Nanoscale

PAPER

View Article Online
View Journal | View Issue

Check for updates

Cite this: *Nanoscale*, 2024, **16**, 10645

An oxygen vacancy-rich BiO_{2-x}/COF heterojunction for photocatalytic degradation of diclofenac†

Yuze Wu,[a] Jingchao Liu,[b] Jinxia Zhao,[a] Chunhong Jin,[a] Hailong Ren,[a] Yilin Yin*[a] and Zenghe Li*[a]

Received 10th February 2024,
Accepted 11th April 2024

DOI: 10.1039/d4nr00608a

rsc.li/nanoscale

A BiO_{2-x}/COF composite was successfully synthesized by simple mechanical ball milling. Compared to pure BiO_{2-x} and COFs, the BiO_{2-x}/COF composite (1 : 9) showed superior photocatalytic capability. Under visible light irradiation for 90 min, the photocatalytic degradation rate of DCF reached 97%. In addition, the characterization results showed that the formation of heterojunctions and the increase in oxygen vacancy concentration were the reasons for the enhancement of the photocatalytic activity. It is confirmed by free radical capture experiments that $^{\bullet}O_2^-$ and h^+ are the main reactive substances in the photocatalytic process. The photocatalytic degradation mechanism of the composite and the photocatalytic degradation pathway of diclofenac were deduced.

Published on 13 April 2024. Downloaded on 5/28/2026 12:35:31 PM.

1. Introduction

The rapid development of technology and industrialization in recent years has drawn attention to two major crises: environmental pollution and energy shortage. Among these concerns, sodium diclofenac (DCF) is a frequently used non-steroidal anti-inflammatory medication.[1–4] It is a widely used medication that has been found to be ecotoxic to both terrestrial and aquatic organisms. It has extremely low biodegradability and its removal rate in wastewater treatment plants is very low, which explains its presence in water bodies. At a concentration as low as 1 μg L^{-1}, diclofenac has been shown to cause renal failure in scavenger animals such as vultures, alter the gills of rainbow trout, and result in tissue damage to fish. This poses a great threat to both human health and the natural ecosystem. Sustainable technologies, such as photocatalytic degradation, show great potential for treating pollutants under sunlight radiation and have therefore attracted extensive attention.[5–7]

Not long ago, BiO_{2-x} was reported to have a narrower band gap and a favorable response to visible light, even extending up to 850 nm, which requires only a simple one-step hydrothermal method to synthesise semiconductor catalysts rich in oxygen vacancies.[8–10] Taking these advantages into account, BiO_{2-x} is being researched as a highly effective photocatalyst for degrading pollutants and inactivating bacteria when exposed to visible light.[11,12] However, due to its narrow band gap, it is easier to recombine photogenerated electron–holes. Some scholars have also utilized bismuth-containing semiconductor materials to enhance the recombination of photocatalytic carriers by constructing heterojunctions, thereby improving the photocatalytic efficiency and offering a novel approach to the modification of BiO_{2-x}.[13–16] Therefore, many studies have modified BiO_{2-x} to improve its photocatalytic activity.[17–19] It has been reported that the photocatalytic activity of BiO_{2-x} can be further improved by adjusting the thickness and Ni doping.[10,20] Chen *et al.* used N-doped GQDs to modify BiO_{2-x} to enhance its response to the full spectrum.[21] The photocatalytic performance can also be improved by forming heterojunctions to inhibit the recombination of electron–hole pairs. For example, Jia *et al.*[22] prepared $(BiO)_2CO_3$/BiO_{2-x}/graphene photocatalysts and Liu *et al.*[23] constructed Z-scheme BiO_{2-x}/BiOBr photocatalysts; both materials exhibited higher photocatalytic activity and stability, which can be attributed to the improved efficiency of charge separation and transfer.

COFs have good application prospects in the degradation of pollutants because of their open and designable structure.[24–27] Many 2D COFs have graphene-like π–π conjugate structures, and the existence of delocalized π bonds enables the COF to have a high carrier transport speed in the stacking direction, which is extremely beneficial for the photocatalytic reaction. They feature adjustable voids, large conjugated structures conducive to electron transfer, and strong absorption of visible light. They are often combined with other semiconductor photocatalysts to increase the specific surface area, enhance visible light absorption, and promote electron transfer. Zhang *et al.*[28] modified 2D BiOBr and 2D TzDa covalent organic

[a]*Beijing University of Chemical Technology, Beijing 100029, China. E-mail: lizh@mail.buct.edu.cn, yinyilin361@163.com*
[b]*School of Computer Science and Engineering, Beihang University, Beijing 100191, China. E-mail: jingchaoliu1992@163.com*

† Electronic supplementary information (ESI) available. See DOI: https://doi.org/10.1039/d4nr00608a

Published on 13 April 2024. Downloaded on 5/28/2026 12:35:31 PM.

frameworks (COFs) by the hydrothermal method and designed an efficient Z-type heterojunction photocatalyst, which is of great significance for solar energy wastewater purification. Based on this property, COFs are commonly used in combination with other semiconductor photocatalysts to enhance their specific surface area, improve visible light absorption, and facilitate electron transfer.[29–31] Therefore, in this study, we synthesized a BiO_{2-x}/COF composite material. Taking diclofenac as an example, the photocatalytic degradation performance and stability of the composite were evaluated. Photocatalytic carriers were further investigated and the band structure was calculated. The mechanism of enhancement of BiO_{2-x}/COF photocatalytic activity and the degradation pathway of diclofenac are discussed.

2. Experimental

2.1 Preparation of photocatalysts

2.1.1 Synthesis of BiO_{2-x}. 0.5039 g of $NaBiO_3$ was dispersed in 20 mL of NaOH (3 M) solution and stirred for 30 min. The above solution was slowly dispersed in 20 mL of deionized water and stirred for 30 min to obtain a suspension. The suspension was transferred into the inner lining of the reactor and heated at 180 °C for 6 hours then cooled to room temperature. After centrifuging the collected products, they were washed with distilled water 5 times and dried at 70 °C.

2.1.2 Synthesis of Py-2,2′-BPyPh COF (COF). 0.0764 mmol 4,4′,4″,4‴-(pyrene-1,3,6,8 tetrayl)tetraaniline (PyTTA), 0.1529 mmol 2,2′-bipyridine-5,5′-diformaldehyde (2,2′-BPyDCA), 1 mL of 1,4-dioxane and 0.1 mL of acetic acid (6 M) were added to a 5 mL high temperature and high pressure resistant glass tube and subjected to ultrasound for 5 min. The reaction mixture was heated at 120 °C for 3 days without disturbance, resulting in the formation of a red solid. The solid was isolated by filtration and washed with dry tetrahydrofuran and dry acetone. The resulting yellow fluffy powder was then dried at 120 °C under vacuum for 12 hours before any characterization was conducted. The resulting composite material is denoted as a COF.

2.1.3 Synthesis of BiO_{2-x}/COF. By utilizing a ball milling method (Scheme 1), we have successfully synthesized composite materials of COFs and BiO_{2-x} with different proportions. The obtained ratios are 0.5COF : 9.5BiO_{2-x}, 1COF : 9BiO_{2-x}, 1.5COF : 8.5BiO_{2-x}, and 2COF : 8BiO_{2-x}.

2.2 Characterization

The phase composition of the sample was studied by X-ray diffraction (XRD, D8A25). The structural forms and elemental distribution of the samples were analyzed through scanning electron microscopy (SEM; ZEISS GeminiSEM 300) and transmission electron microscopy (TEM; FEI Talos F200x) complemented by energy-dispersive X-ray spectroscopy (EDS) in detail. Fourier transform infrared (FT-IR) spectra were obtained using a Nicolet 6700 Fourier transform infrared spectrometer to study the chemical bond properties of the samples. The elemental surface distribution of the samples was ascertained using X-ray photoelectron spectroscopy (XPS; Thermo Scientific K-Alpha). UV-visible diffuse reflectance spectroscopy (UV-vis DRS) spectra were obtained using a UV-3600 ultraviolet–visible spectrophotometer. Photoluminescence spectra were recorded using a HITACHI F-7000 fluorescence spectrophotometer. Electrochemical impedance spectroscopy (EIS), Mott–Schottky analysis (M–S), and photocurrent measurements (i–t) were carried out using an electrochemical workstation (Shanghai Chenhua). Platinum electrodes and Ag/AgCl electrodes were used as working and reference electrodes, respectively, with a 0.1 M Na_2SO_4 electrolyte. The preparation of the working electrode involved the deposition of 220 μL of a suspension (2 mg of the catalyst dispersed in 200 μL of ethanol and 20 μL of Nafion mixed solution) onto a 1 × 1 cm^2

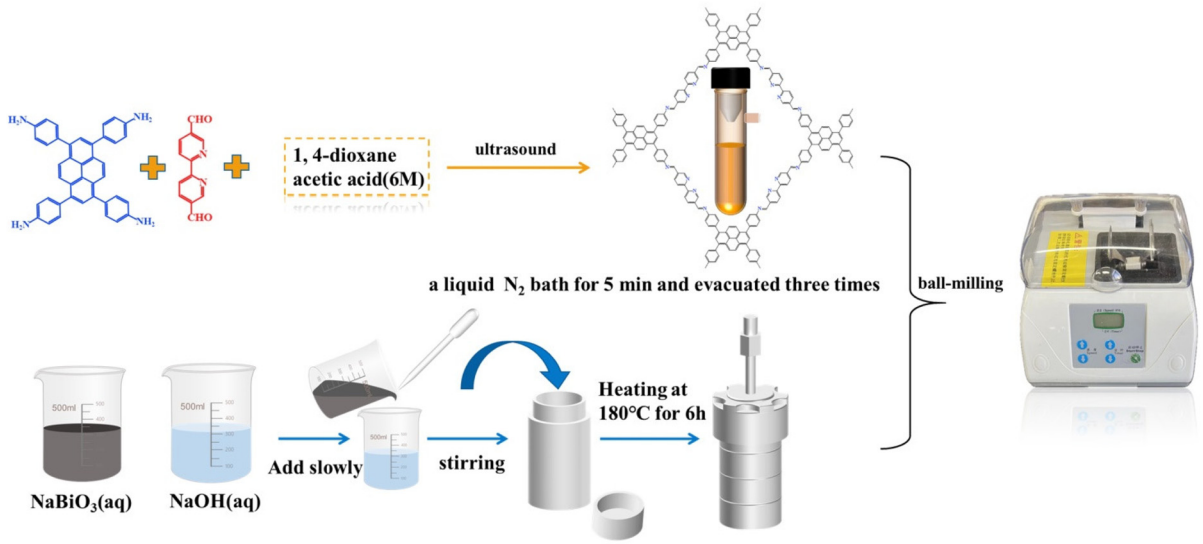

Scheme 1 Synthetic steps of BiO_{2-x}/COF.

This journal is © The Royal Society of Chemistry 2024

Published on 13 April 2024. Downloaded on 5/28/2026 12:35:31 PM.

FTO glass substrate, followed by drying at 60 °C. To detect the presence of oxygen vacancies and the formation of a superoxide, electron paramagnetic resonance (EPR) signals were recorded using a Bruker EMXplus spectrometer and hydroxide radicals in the photocatalytic reaction system with DMPO as a spin-trapped reagent at a concentration of 0.2 M.

2.3 Photocatalytic tests

Using a 300 W xenon lamp (λ > 420 nm, CEL-HXF300) as a light source, the photocatalytic performance of the composite was investigated by the degradation of diclofenac (DCF) under visible light irradiation. The specific reaction system is as follows: 50 mg of the photocatalyst was added to 50 mL of DCF aqueous solution (20 mg L^{-1}), dispersed evenly, and stirred in the dark for 40 min to reach equilibrium. After that, the light source was turned on, samples were taken once every 10 min, and a 0.45 μm microporous filter membrane was used for filtration to remove the catalyst in the obtained solution.

2.4 Analytical methods

Diclofenac was quantitatively analyzed by high-performance liquid chromatography (HPLC). The detection conditions were as follows: C18 column (5 μm, 4.6 mm × 254 mm), PDA detector, detection wavelength 276 nm, mobile phase methanol : 2‰ acetic acid aqueous solution = 80 : 20, flow rate 1.0 mL min^{-1}, and sample size 20 μL. The product of the DCF degradation pathway was detected using LC-MS (UPLC/Premier); a triple quadrupole detector equipped with an electrospray ionization (ESI) source was utilized for analysis. The scan range was extended from m/z 50 to 400. Methanol/0.1% formic acid aqueous solution (80/20) was selected as the mobile phase.

3. Results and discussion

First, the synthesized materials were characterized. Fig. 1(a) presents the XRD diffraction patterns of BiO_{2-x} combined with COFs of different weights. The characteristic XRD peaks at 2θ = 28.01°, 32.69°, 46.91°, 55.64°, 58.33° and 68.51° are ascribed to the (111), (200), (220), (311), (222) and (400) planes, respectively. This is consistent with the characteristic peak of the BiO_{2-x} standard card (JCPDS no. 47-1097).[10] The characteristic peak of the COF also appeared at 3.1° (Fig. S1†), indicating that the synthesized BiO_{2-x}, COF and corresponding composites had good crystal shape, indicating that the synthesis was successful. However, no COF peak was found in the composite materials, and it was speculated that the COF content in the composite material was less. Therefore the COF was compounded with BiO_{2-x} in a ratio of 9 : 1 and the peak of the COF was obtained, which successfully confirmed the conjecture. Fig. 1b shows the FTIR spectra of the COF, BiO_{2-x} and 1COF : 9BiO_{2-x}, which were used to determine the chemical composition of 1COF : 9BiO_{2-x}. The positions of the characteristic peaks of the composite were consistent with those of the COF and BiO_{2-x}, wherein 1621 cm^{-1} comes from the stretching vibration of the imine bond of the COF,[32] and 592 cm^{-1} and 533 cm^{-1} correspond to the Bi–O bond vibration characteristic peaks of BiO_{2-x},[33,34] In comparison, BiO_{2-x} and the COF can be identified in the BiO_{2-x}/COF composites. With the increase of COF content, the absorption band strength of the COF gradually increases, while that of BiO_{2-x} relatively decreases, further demonstrating the coexistence of the two contents of BiO_{2-x} and the COF in the composite materials.

Fig. 2(a) shows the scanning electron microscopy image of BiO_{2-x}, and it can be seen that the synthesized BiO_{2-x} has a small fragment morphology.[35] Fig. 2(b) shows the SEM image of the COF,[32] and it can be clearly seen that the COF is a sheet material. As shown in Fig. 2(c), BiO_{2-x} is uniformly dispersed on the surface of the COF, and from the mapping images in Fig. 2(g), (h), (i) and (j), the Bi, O, N and C elements of 1COF : 9BiO_{2-x} are uniformly distributed. This indicates that BiO_{2-x} and the flake structure of the COF are tightly bound in the composite material. Fig. 2(d) shows the TEM image of 1COF : 9BiO_{2-x}. It clearly shows the tight attachment of BiO_{2-x} small fragments to the surface of COF nanosheets, indicating the formation of a well-defined heterojunction between BiO_{2-x}

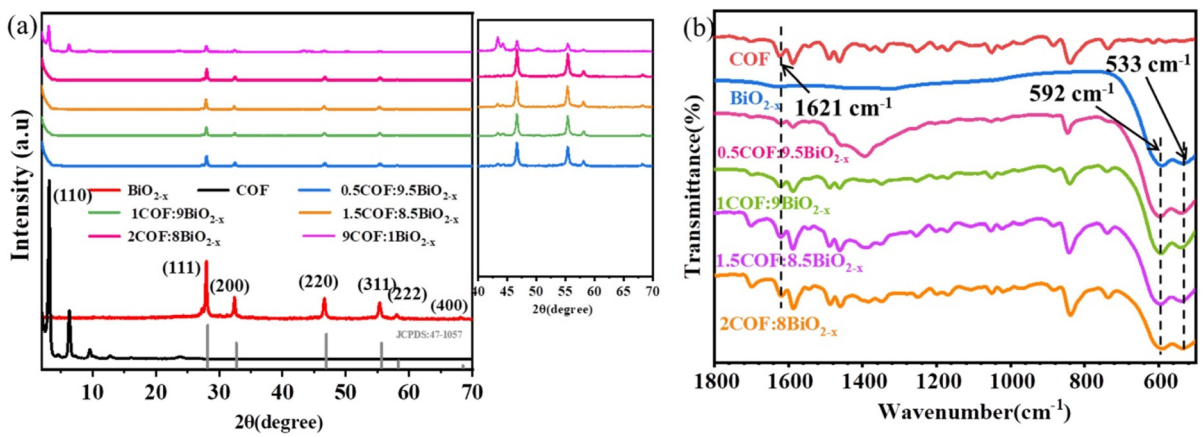

Fig. 1 (a) XRD patterns of BiO_{2-x} combined with COFs of different weights; (b) Infrared images of BiO_{2-x} combined with COF of different weight.

Published on 13 April 2024. Downloaded on 5/28/2026 12:35:31 PM.

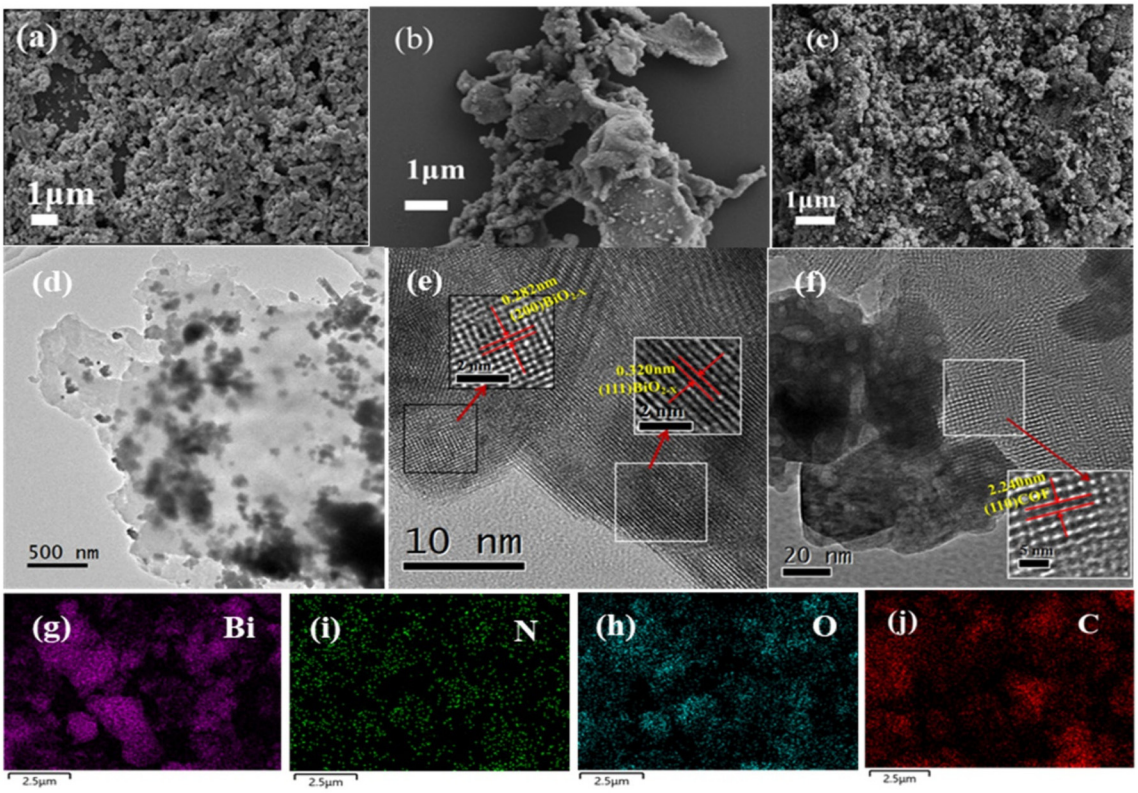

Fig. 2 SEM images of (a) BiO_{2-x}, (b) COF, and (c) 1COF : 9BiO_{2-x}; (d) TEM image of the 1COF : 9BiO_{2-x} sample; (e and f) HRTEM image of 1COF : 9BiO_{2-x}; and (g)–(j) mapping images of 1COF : 9BiO_{2-x}.

and the COF. The HRTEM images are presented in Fig. 2(e) and (f) for the 1COF : 9BiO_{2-x} composite material. The crystal plane (110) of the COF can be clearly seen in the 20 nm scale, corresponding to a lattice spacing of 2.240 nm; this result further shows that the reason why the composites do not show the diffraction peak of the COF in XRD is that the COF content is less. Fig. 2(e) shows a local magnification of Fig. 2(f), and it can be clearly observed that lattice fringe spacing of 0.320 and 0.282 nm corresponds to the (111) and (200) lattice planes of BiO_{2-x}, respectively.[22,36] The HRTEM images provided further evidence of the coexistence of BiO_{2-x} and the COF, as well as the formation of an interfacial heterojunction. Through the above characterization, it is further concluded that the two semiconductors are closely combined.

The surface compositions and chemical states of pure BiO_{2-x}, COF and 1COF : 9BiO_{2-x} samples were analyzed by XPS. Fig. 3(a) shows the XPS survey spectra of BiO_{2-x}, the COF, and 1COF : 9BiO_{2-x}. Compared with pure BiO_{2-x} and the COF, four elements C, N, O and Bi can be observed in the composite material, and no other impurity elements can be observed in the spectrum. Fig. 3(b) shows the XPS spectral comparison of the O1s peaks of BiO_{2-x}, the COF and 1COF : 9BiO_{2-x}. It can be seen from the figure that the positions of the peaks of the composite material change relative to pure BiO_{2-x} and the COF. First, the C 1s spectrum was analyzed. In the spectrum, the peaks at 284.8 eV, 285.6 eV, and 288.6 eV correspond to C═C, C═N, and C═O functionalities, respectively (Fig. S2†). There are three O 1s peaks at 529.7 eV, 531.2 eV and 532.5 eV,[10,37,38] which can be assigned to the lattice oxygen, surface oxygen vacancies and surface adsorbed oxygen, respectively. Fig. 3(c) shows the Bi 4f spectrum of the composite material that has two peaks at 164.5/163.8 eV and 159.1/158.5 eV, which were attributed to Bi $4f_{7/2}$ and Bi $4f_{5/2}$, respectively. Compared with pure BiO_{2-x}, the XPS peak of Bi 4f shifted to higher binding energy. Fig. 3(d) shows the N 1s spectrum of the composite material that has a peak at 399.1 eV, which moves toward the lower binding energy relative to the binding energy of the N 1s spectrum in the COF, indicating that there is electron transfer at the interface of the two materials, electrons move from high binding energy to low binding energy, and electrons move from the BiO_{2-x} surface to the COF surface. The two materials are highly bonded.

To further analyse the oxygen vacancies in the catalyst, the EPR test was conducted on BiO_{2-x}, the COF and the 1COF : 9BiO_{2-x} composite. As shown in Fig. 4(a), it can be seen that BiO_{2-x} has a large and wide peak with g = 2.05.[10,37–39] This is attributed to bismuth defects caused by oxygen vacancies in the photocatalytic material. The EPR signal becomes stronger after compositing, indicating that the oxygen vacancy concentration increases after compositing, which is also conducive to the improvement of photocatalytic degradation performance. The embedded figure is a compari-

 This journal is © The Royal Society of Chemistry 2024

Published on 13 April 2024. Downloaded on 5/28/2026 12:35:31 PM.

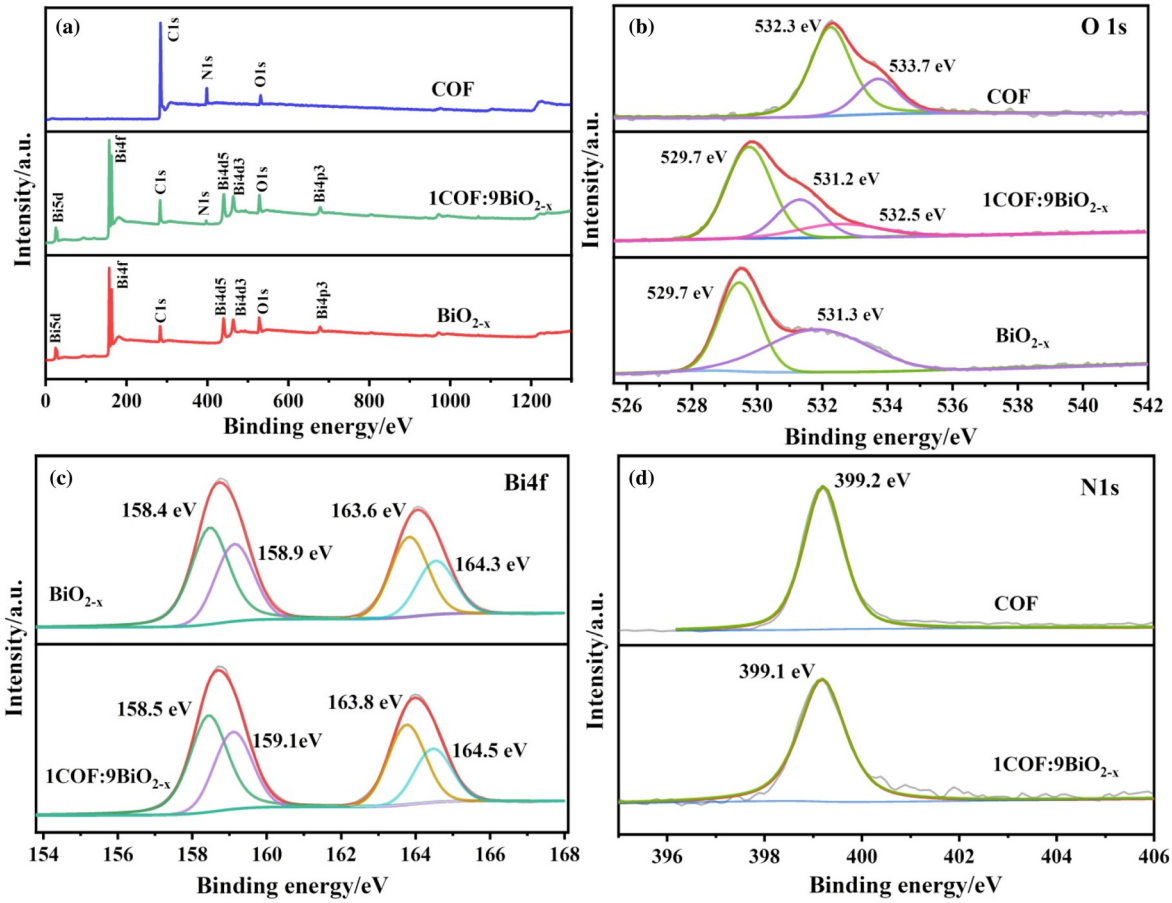

Fig. 3 XPS spectra of BiO_{2-x}, the COF and 1COF : $9BiO_{2-x}$: (a) survey, (b) O 1s, (c) Bi 4f, and (d) N 1s.

son between the enlarged yellow region of the composite material and the EPR of the COF. It can be clearly seen from the figure that the COF can detect vibration signals at g = 2.003, indicating that the COF also has oxygen vacancies,[40] and the EPR signal of the composite has a wide peak of bismuth defects caused by oxygen vacancies at g = 2.05. There is also an oxygen vacancy peak of g = 2.004. It is further proved that the composite material has oxygen vacancies. This conclusion is consistent with the previous XPS spectrogram of O 1s, which confirms that the prepared oxygen vacancies are also conducive to improving the photocatalytic performance.[41]

The optical properties of BiO_{2-x}, the COF and the 1COF : $9BiO_{2-x}$ composite can be obtained from UV-visible diffuse reflectance spectra (DRS), the light absorption intensity and the range of the catalyst can be evaluated, and the band gap of the corresponding materials can be calculated according to the Tauc plot formula. The redshift of the strongest absorption peak of the composite material was obtained from Fig. 4(b), and the light absorption capacity of the composite material was enhanced compared with that of pure BiO_{2-x}, indicating that its absorption of visible light was also improved. Fig. 4(c) and (d) show the band gap widths (E_g) of the COF and BiO_{2-x} calculated according to the Tauc plot formula, which are 2.26 eV and 1.62 eV, respectively.

After the successful synthesis of the material, which was confirmed by the characterization method, the performance of the catalyst was tested. Under visible light irradiation, diclofenac was photocatalyzed to evaluate the photocatalytic performance of composites with different weight ratios, and DCF was quantitatively analysed using high-performance liquid chromatography. As shown in Fig. 5(a), the composite ratio with the best photocatalytic degradation performance is 1 : 9, and with an increase in the amount of COF, the adsorption in the dark reaction stage is enhanced, which is also attributed to the advantage of the large specific surface area of the COF. The degradation rate of the composite ratio of 1 : 9 reaches 96% at 60 min and 97% at 90 min, and the optimal composite ratio is 1 : 9. Compared with BiO_{2-x}, the photocatalytic performance of the 1COF : $9BiO_{2-x}$ composite is better. Blank control experiments were also conducted to confirm the importance of illumination (Fig. S3†).

In addition to assessing the photocatalytic efficacy, the kinetics of DCF degradation under photocatalysis was investigated. It was postulated that the degradation of DCF by different materials follows first-order reaction kinetics, and kinetic modeling was conducted based on the corresponding rate equations.

Published on 13 April 2024. Downloaded on 5/28/2026 12:35:31 PM.

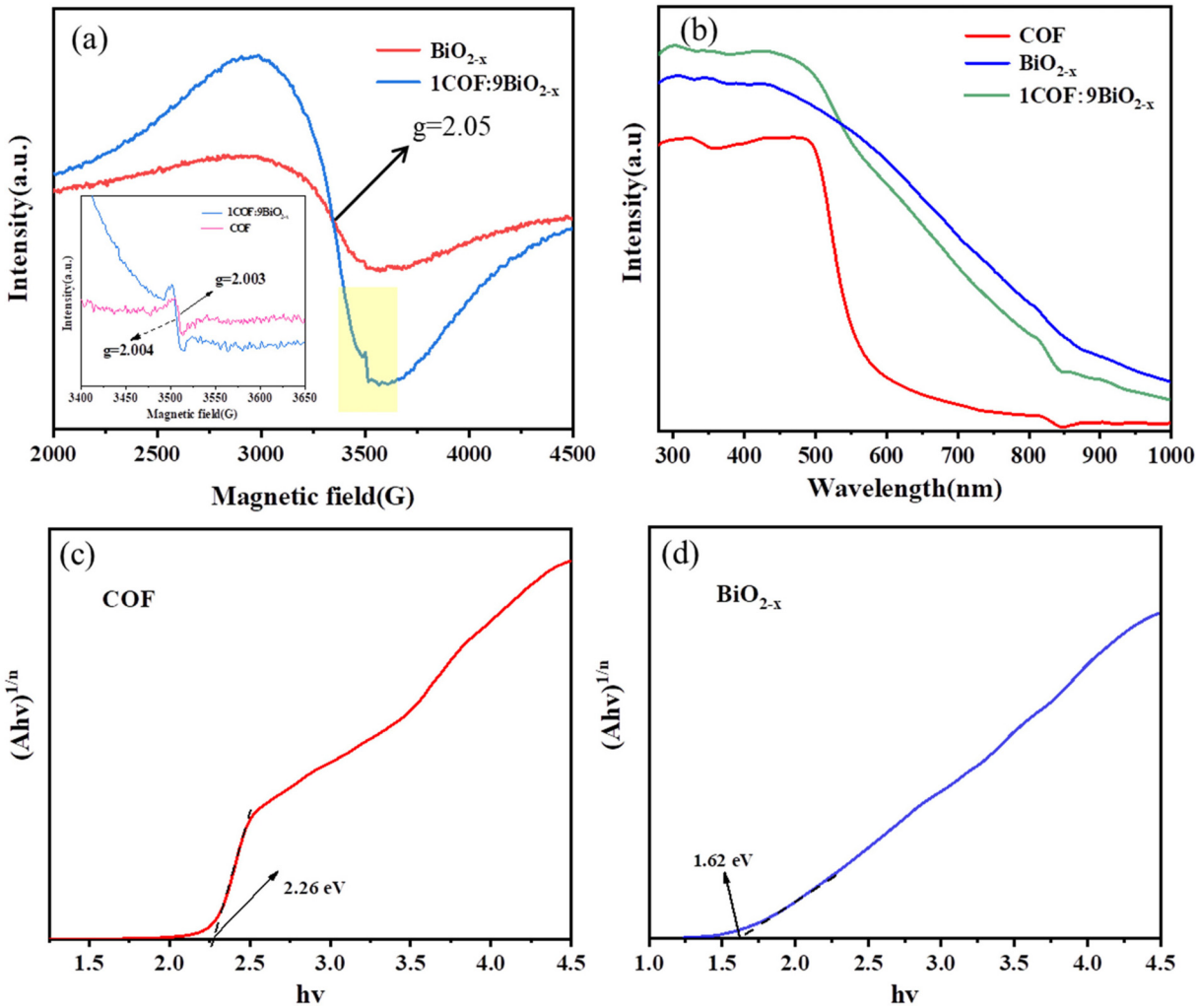

Fig. 4 (a) EPR spectra of BiO_{2-x}, the COF and the 1COF : 9BiO_{2-x} catalyst; (b) UV-vis absorption spectra of the COF, BiO_{2-x} and the 1COF : 9 BiO_{2-x} composite; and (c and d) energy band gaps of the COF and BiO_{2-x}.

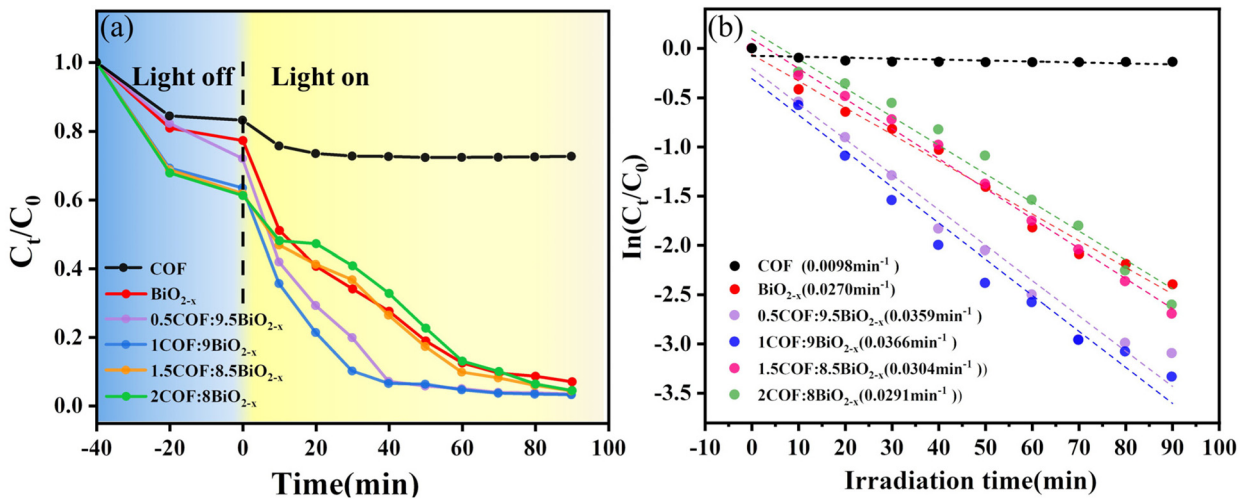

Fig. 5 (a) Photocatalytic degradation of DCF by BiO_{2-x} with composites of different weights; (b) DCF rate constant diagram of the photocatalytic degradation of BiO_{2-x} with composites of different weights.

This journal is © The Royal Society of Chemistry 2024

Published on 13 April 2024. Downloaded on 5/28/2026 12:35:31 PM.

The degradation of diclofenac was similarly assumed to adhere to first-order kinetics and was fitted accordingly using the kinetic equation. As shown in Fig. 5(b), the degradation kinetics is first-order, the reaction rate constant is obtained, and the reaction rate constant of the 1COF : 9BiO_{2-x} composite is the highest.

In addition to evaluating the photocatalytic performance of the catalyst, its stability is also an important property for long-term use in practical applications. In order to assess the stability of the composite photocatalyst, the recycling experiment was performed four times over the composite. As shown in Fig. 6(a), the material can be recycled four times, and the photocatalytic degradation performance of the 1COF : 9BiO_{2-x} composite decreases after four cycles, which may due to the loss of some solids in each cycle experiment. The amount of the photocatalyst is reduced. However, 97% of the degradation effect is still achieved after four cycles, indicating that the catalyst shows good physical and chemical stability and good recyclability. In order to better verify this, XRD and IR were conducted after four cycles, as shown in Fig. 6(b) and (c). It can be seen that the IR data and XRD patterns of 1COF : 9BiO_{2-x} before and after four cycles are basically consistent, indicating that the catalyst has good stability, which is of great value for the practical application of the material.

To elucidate the mechanism behind the improvement of photocatalytic activity, two main factors affecting the photocatalytic performance of light absorption and charge separation were studied. The photochemical properties of the catalyst were assessed using the transient photocurrent response and electrochemical impedance spectroscopy (EIS). The transient photocurrent value provided a direct indication of the separation efficiency and migration rate of the photoinduced charge carriers. Fig. 7(a) shows that the transient photocurrent response of 1COF : 9BiO_{2-x} increases significantly, showing the best photoresponse performance, which proves that under visible light irradiation, 1COF : 9BiO_{2-x} has higher carrier separation efficiency than BiO_{2-x}.

The results of electrochemical impedance spectroscopy and photocurrent density test are consistent, indicating that the effective electron transfer in 1COF : 9BiO_{2-x} is the main reason for its excellent photocatalytic activity. EIS is commonly used to study the separation efficiency of electrons and holes in photocatalytic reactions. As shown in Fig. 7(b), the EIS Nyquist plot of the 1COF : 9BiO_{2-x} composite is significantly smaller than that of other composites, indicating that after the appropriate combination of BiO_{2-x} and the COF, the charge transfer resistance is reduced and the photogenerated electrons and hole recombination rate are reduced, which proves that the improvement of its photocatalytic ability under visible light promotes the photocatalytic degradation reaction. In addition, fluorescence photoluminescence spectra can be used to evaluate the electron and hole recombination efficiency of the material, and the stronger the fluorescence intensity, the more easily the photogenerated electrons and holes recombine. As shown in Fig. 7(c), comparatively, it can be clearly found that the PL emission intensity of the composite (1COF : 9BiO_{2-x}) exhibited a significant decrease in recombination, indicating that the coupling of BiO_{2-x} and the COF effectively suppressed the recombination of photogenerated electron–hole pairs.[42]

Before the mechanism of photocatalytic oxidation of DCF was proposed, free radical trapping experiments and EPR were performed to determine the types of active species and their respective contributions. In these trapping experiments, EDTA disodium salt (EDTA-2Na) was used to trap photogenerated h^+, isopropyl alcohol (IPA) was used to trap hydroxide radicals ($^{\bullet}OH$), and vitamin E and $AgNO_3$ were selected to trap the superoxide anion radical ($^{\bullet}O_2^-$) and e^-, respectively. As shown in Fig. 7(d), the degradation rate of diclofenac decreased when EDTA-2Na and vitamin E were added to the photocatalytic reaction, and the main active species of diclofenac were h^+ and $^{\bullet}O_2^-$. Moreover, after adding $AgNO_3$, the degradation rate of the photocatalyst was improved, indicating that the content of h^+ increases after the trapping agent captures e^-, so the photocatalytic rate increases, which also reflects that h^+ is the main active species.

Under simulated experimental conditions, the existence of $^{\bullet}O_2^-$ radicals in the reaction system was confirmed by electron spin resonance (EPR). As shown in Fig. 7(e), almost no signal was observed when the system was in the dark, indicating that 1COF : 9BiO_{2-x} could not produce $^{\bullet}O_2^-$ under dark conditions. The EPR signal of DMPO-$^{\bullet}O_2^-$ can be clearly observed after 5 min of illumination, and the signal intensity of DMPO-$^{\bullet}O_2^-$

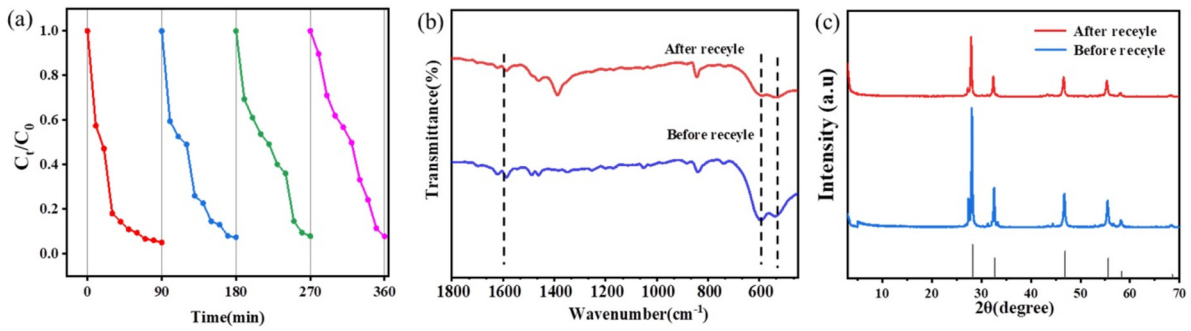

Fig. 6 (a) 1COF : 9BiO_{2-x} catalysed by visible light for 4 cycles and FT-IR spectra (b) and XRD patterns (c) of 1COF : 9BiO_{2-x} obtained before and after the reaction.

Published on 13 April 2024. Downloaded on 5/28/2026 12:35:31 PM.

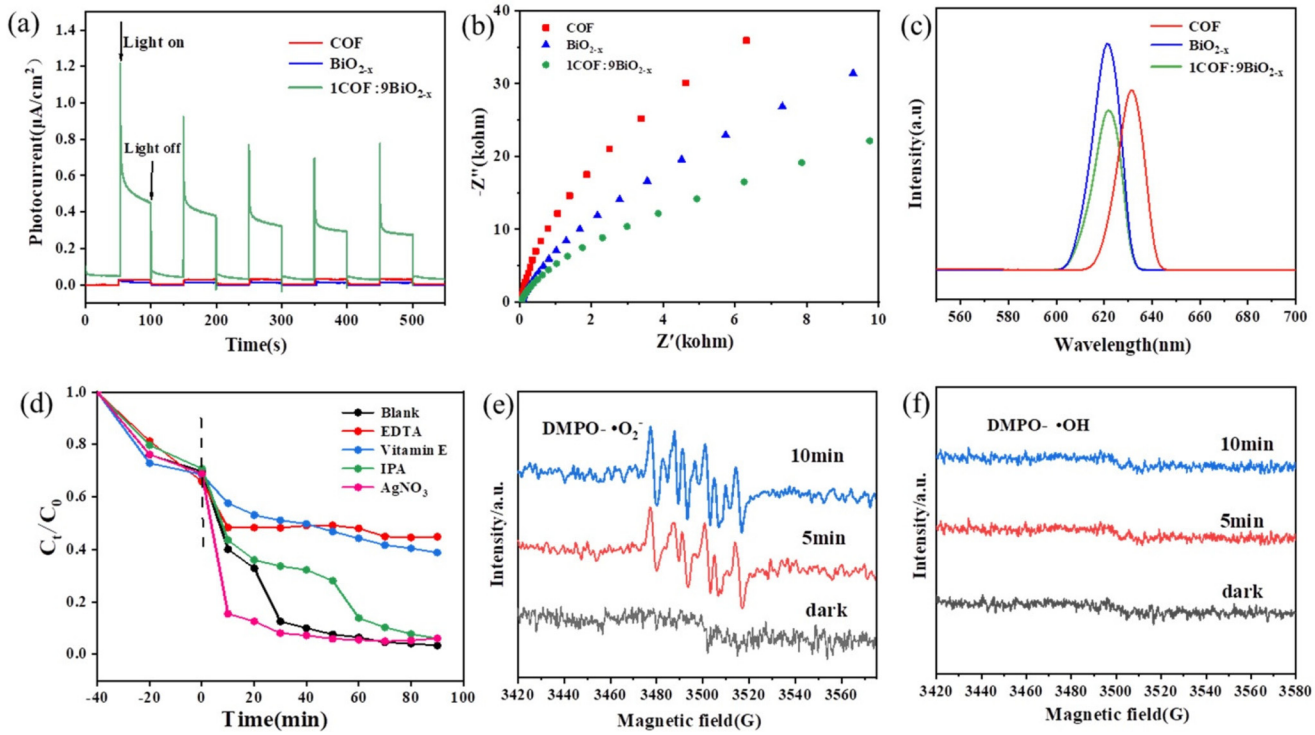

Fig. 7 (a) Transient photocurrent responses, (b) EIS Nyquist plots and (c) PL spectra of the COF, BiO_{2-x} and 1COF : $9BiO_{2-x}$; (d) radical capture experiment; and EPR diagrams of 1COF : $9BiO_{2-x}$ DMPO-$^{\cdot}O_2^-$ (e) and DMPO-$^{\cdot}$OH (f) under visible light irradiation.

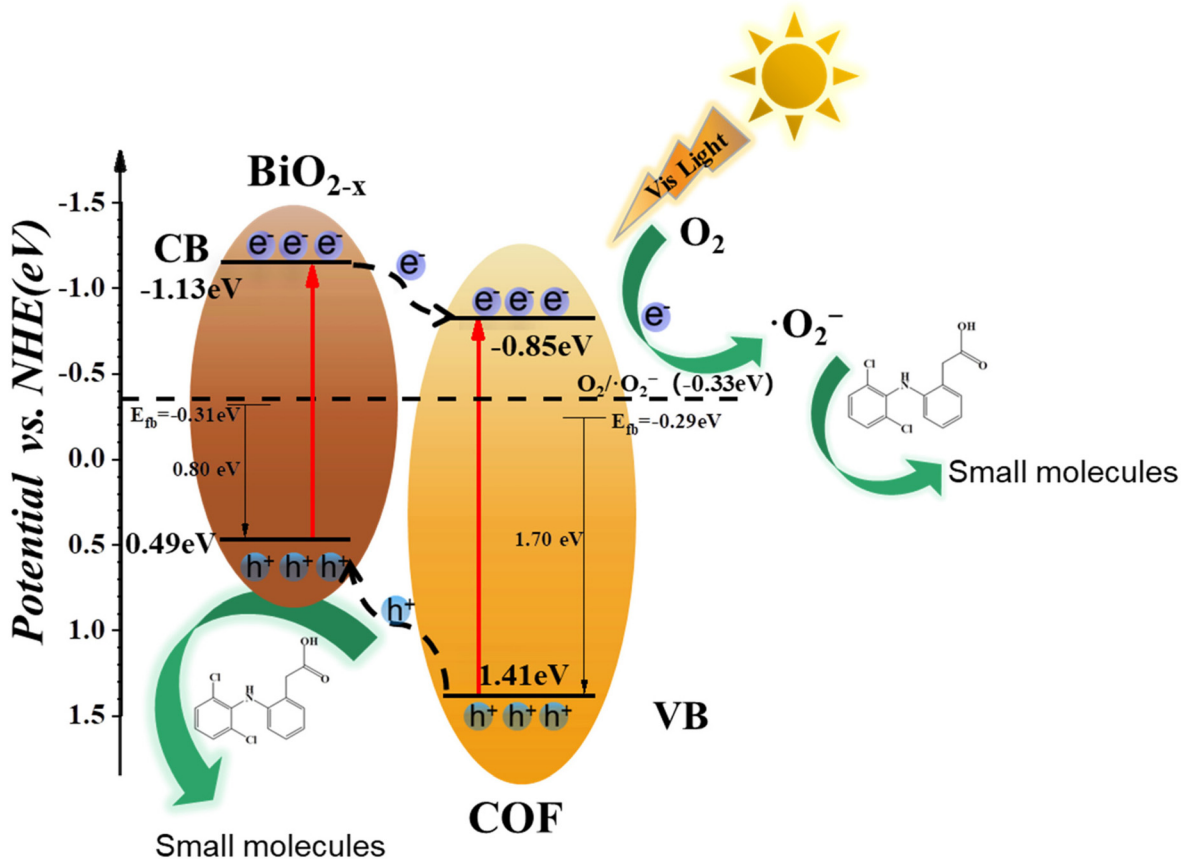

Fig. 8 Mechanism diagram of the photocatalytic degradation of DCF by the BiO_{2-x}/COF heterojunction under visible light irradiation.

This journal is © The Royal Society of Chemistry 2024

Published on 13 April 2024. Downloaded on 5/28/2026 12:35:31 PM.

increases with the increase of illumination time. The results indicated that 1COF : 9BiO_{2-x} could produce $^{\bullet}O_2^-$ under illumination. As shown in Fig. 7(f), DMPO-$^{\bullet}$OH was not detected under either dark or light conditions, indicating that the catalyst could not produce $^{\bullet}$OH. This is consistent with the results obtained from the trapping experiments.

After identifying the active species, Mott–Schottky (M–S) analysis and valence band XPS spectra were employed to calculate the relative positions of the conduction band (CB) and the valence band (VB) of the COF and BiO_{2-x}. As shown in Fig. S4(a) and (b),† the slope of M–S is positive, indicating that BiO_{2-x} and the COF are n-type semiconductors. This shows that the Fermi level (EF) is equivalent to the flat band potential (E_{fb}).[43] The Mott–Schottky plots, which mean the Fermi energy level (EF) of BiO_{2-x} and the COF, can be obtained from the intercept on the horizontal coordinate as −0.53 eV and −0.51 eV (*vs.* Ag/AgCl) (−0.31 eV and −0.29 eV (*vs.* NHE)), respectively. The distance between the maximum value of the VB and the Fermi level can be determined by the valence band XPS spectra, as shown in Fig. S5(a) and (b).†[33] The distance between BiO_{2-x} and the COF is about 0.80 eV and 1.70 eV, respectively. The VB potentials of BiO_{2-x} and the COF are 0.49 eV and 1.41 eV (*vs.* NHE), respectively, and the CB potentials are −1.13 eV and −0.85 eV (*vs.* NHE), respectively.[34,44] The band potentials of BiO_{2-x} and the COF exhibit a staggered band alignment, resulting in an energy bias naturally generated at the contact interfaces between these materials in the composite. This energy bias facilitates the separation and transfer of photogenerated carriers in the system.

According to the above experimental results and discussion, the photocatalytic degradation mechanism of BiO_{2-x}/COF on DCF in water was proposed. As shown in Fig. 8, under visible light irradiation, both the COF and BiO_{2-x} can be excited, generating e^- and h^+. Due to the band energy difference between the COF and BiO_{2-x}, photogenerated electrons in the conduction band (CB) of BiO_{2-x} tend to migrate to the CB of the COF, while h^+ in the valence band (VB) of the COF move to the VB of BiO_{2-x}. This directional carrier migration effectively inhibits the recombination of electron–hole pairs and enhances the photocatalytic activity of the whole system. In addition, considering that CB potentials of BiO_{2-x} and the COF (−1.13 eV and −0.85 eV) are more negative than those of E^{θ} (O_2/$^{\bullet}O_2^-$) (−0.33 eV *vs.* NHE), the electrons in the CB of the COF can be reduced to $^{\bullet}O_2^-$ through a one-electron reducing reaction. The DCF

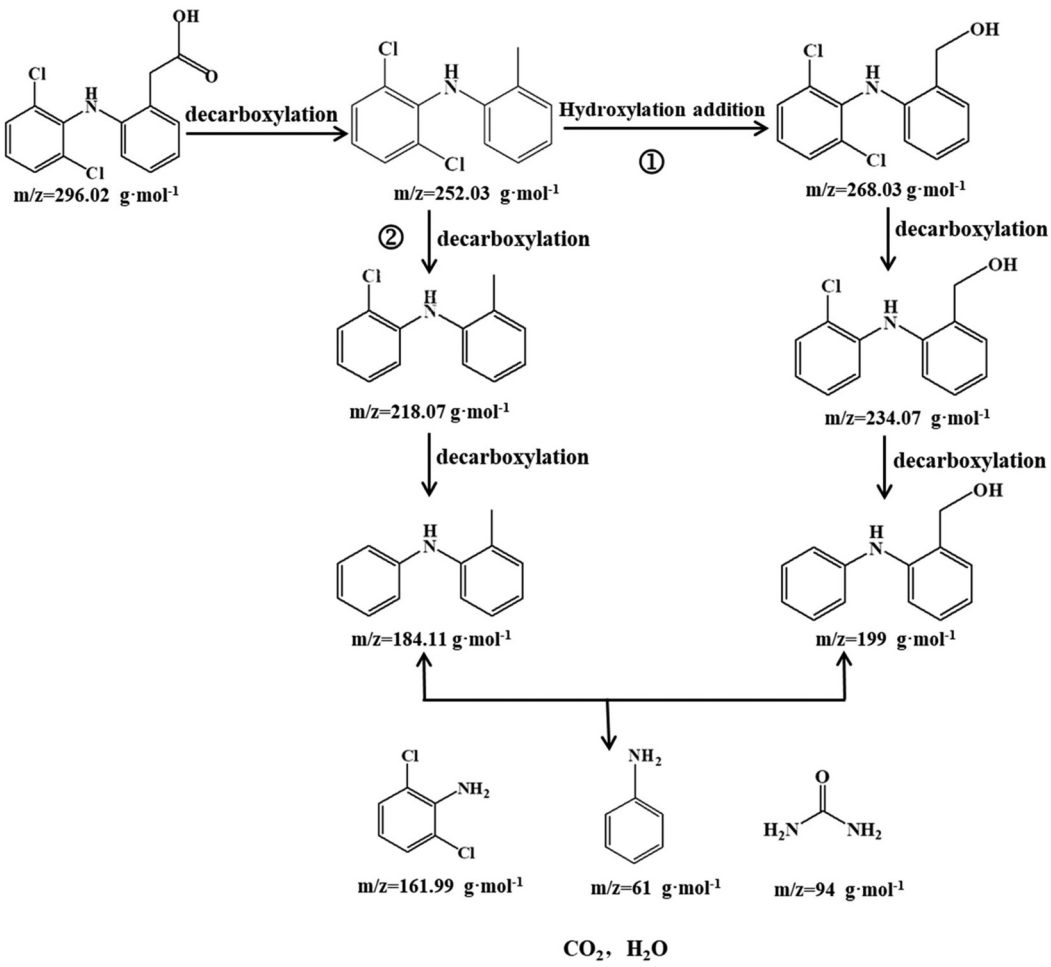

Scheme 2 Theprobable degradation mechanism for diclofenac degradation.

Published on 13 April 2024. Downloaded on 5/28/2026 12:35:31 PM.

adsorbed on the surface of the BiO_{2-x}/COF catalyst is oxidized and degraded under the action of $^{\bullet}O_2^-$, while the strong oxidizing h^+ located on the VB of BiO_{2-x} can directly oxidize and degrade DCF. The DCF in the final aqueous solution is degraded by the joint action of h^+ and $^{\bullet}O_2^-$, thus achieving the removal of pollutants. In the BiO_{2-x}/COF photocatalyst, the introduction of oxygen vacancies on BiO_{2-x} leads to the reduction of the band gap width of the catalyst, and therefore has a wider range of wavelength response, while the COF acts as a high-quality carrier based on its adsorption performance, carrier transport performance and the presence of oxygen vacancies. The photocatalytic degradation performance of the two materials was improved by forming a traditional type-II heterojunction.

In the evaluation stage of photocatalytic performance, by-products were observed in the degradation process. Based on the kinetic results and the peak conditions (Fig. S6†) of LC-MS, we proposed the mechanism of photocatalytic degradation of DCF, as shown in Scheme 2.[45–49] LC-MS analysis was conducted to determine the formation of photocatalytic intermediates during the irradiation process. In the photocatalytic reaction, BiO_{2-x}/COF is stimulated by light to produce more reactive oxygen species, and the effect of oxidative decarboxylation is enhanced. Diclofenac is preferentially oxidized and decarboxylated to 2,6-dichloro-*N*-*o*-tolyaniline (m/z = 252) under hydroxylation addition, and then produces m/z 234 and 199 products under dechlorination and oxidation. Another degradation pathway was oxidative decarboxylation to 2,6-dichloro-*N*-*o*-tolyaniline (m/z = 252) and dechlorination to an m/z of 218.07 and an m/z of 184.11. These intermediates are eventually degraded into small molecules (m/z = 161.99, m/z = 94, m/z = 61) as well as CO_2 and H_2O.

4. Conclusion

In summary, a kind of BiO_{2-x}/COF heterojunction photocatalyst containing rich oxygen vacancies was successfully prepared by a simple and rapid mechanical ball milling method. The oxygen vacancy of BiO_{2-x} causes Bi defects, which is conducive to molecular oxygen activation. It was combined with a COF with a large specific surface area to form a heterojunction, which greatly inhibited the recombination of photogenerated carriers, and the photocatalytic activity of the prepared BiO_{2-x}/COF photocatalyst was enhanced compared to that of pure BiO_{2-x}. Its excellent photocatalytic performance is attributed to the presence of delocalized π bonds in the COF, which enhances the carrier transport speed and facilitates rapid separation of photo-generated carriers, as well as the synergistic effect between the presence of oxygen-rich vacancies in BiO_{2-x} and the formation of heterojunctions. Under irradiation with visible light for 90 min, the photocatalytic degradation rate of DCF reached 97% and showed good stability. At the same time, BiO_{2-x}/COF also showed high photocatalytic activity for the degradation of tetracycline hydrochloride under visible light (Fig. S7†). In addition, the free radical trapping experiment results showed that h^+ and $^{\bullet}O_2^-$ free radicals were the primary active species responsible for the photodegradation process. In addition to CO_2 and H_2O, there are also some small organic molecules for photocatalytic degradation. This study provides a feasible strategy for the degradation of new pollutants.

Conflicts of interest

The authors declare no competing interests.

Acknowledgements

The authors would like to thank Professor Zenghe Li for providing financial support and guidance.

References

1 Y. Zhang, Y. Zhao, Z. Xiong, T. Gao, B. Gong, P. Liu, J. Liu and J. Zhang, *Appl. Catal., B*, 2021, **282**, 119534.
2 G. M. Neelgund, V. N. Bliznyuk and A. Oki, *Appl. Catal., B*, 2016, **187**, 357–366.
3 W. Li, R. Yu, M. Li, N. Guo, H. Yu and Y. Yu, *Chemosphere*, 2019, **218**, 966–973.
4 S. Cao, J. Low, J. Yu and M. Jaroniec, *Adv. Mater.*, 2015, **27**, 2150–2176.
5 J. Schwaiger, H. Ferling, U. Mallow, H. Wintermayr and R. D. Negele, *Aquat. Toxicol.*, 2004, **68**, 141–150.
6 Y. Zhang, S.-U. Geißen and C. Gal, *Chemosphere*, 2008, **73**, 1151–1161.
7 J. L. Oaks, M. Gilbert, M. Z. Virani, R. T. Watson, C. U. Meteyer, B. A. Rideout, H. L. Shivaprasad, S. Ahmed, M. J. I. Chaudhry, M. Arshad, S. Mahmood, A. Ali and A. A. Khan, *Nature*, 2004, **427**, 630–633.
8 M. Elangovan, S. M. Bharathaiyengar and J. PonnanEttiyappan, *Environ. Sci. Pollut. Res.*, 2021, **28**, 18186–18200.
9 X. Zhang, L. Shi and Y. Zhang, *J. Taiwan Inst. Chem. Eng.*, 2022, **132**, 104111.
10 J. Li, X. Wu, W. Pan, G. Zhang and H. Chen, *Angew. Chem., Int. Ed.*, 2018, **57**, 491–495.
11 H. Sun, K. M. Xiao, Y. F. Ma, S. N. Xiao, Q. T. Zhang, C. L. Su and P. K. Wong, *J. Hazard. Mater.*, 2022, **431**, 128510.
12 H. Luo, T. Jiang, C. Zhan, N. He, L. Tan, F. Jiang and H. Chen, *Environ. Res.*, 2023, **228**, 115854.
13 C. Zhao, X. Li, L. Yue, S. Yuan, X. Ren, Z. Zeng, X. Hu, Y. Wu and Y. He, *J. Alloys Compd.*, 2023, **968**, 171956.
14 C. Zhao, X. Li, L. Yue, X. Ren, S. Yuan, Z. Zeng, X. Hu, Y. Wu and Y. He, *ACS Appl. Nano Mater.*, 2023, **6**, 15709–15720.
15 C. Zhao, X. Li, L. Yue, X. Ren, S. Yuan, Z. Zeng and Y. He, *Mater. Res. Bull.*, 2023, **167**, 112377.

 This journal is © The Royal Society of Chemistry 2024

Published on 13 April 2024. Downloaded on 5/28/2026 12:35:31 PM.

16 S. Yuan, J. Wang, C. Zhao, L. Yue, X. Ren, Z. Zeng, X. Hu, Y. Wu and Y. He, *Sep. Purif. Technol.*, 2023, **325**, 124665.
17 H. Zhang, Z. Fan, Q. Chai and J. Li, *Catalysts*, 2023, **13**, 469.
18 Y. Chen, Z. Han, Z. Liu, Z. Liu and P. Feng, *J. Phys. Chem. Solids*, 2022, **165**, 110692.
19 D. Xu, G. Li, Y. Dong, Q. Wang, J. Zhang, T. Yang, S. Pang, G. Zhang, L. Lv, Y. Xia, Z. Ren and P. Wang, *Appl. Catal., B*, 2022, **312**, 121402.
20 J. Li, J. Wang, G. Zhang, Y. Li and K. Wang, *Appl. Catal., B*, 2018, **234**, 167–177.
21 F. Chen, L. L. Liu, Y. J. Zhang, J. H. Wu, G. X. Huang, Q. Yang, J. J. Chen and H. Q. Yu, *Appl. Catal., B*, 2020, **277**, 119218.
22 Y. F. Jia, S. P. Li, J. Z. Gao, G. Q. Zhu, F. C. Zhang, X. J. Shi, Y. Huang and C. L. Liu, *Appl. Catal., B*, 2019, **240**, 241–252.
23 J. W. Liu, L. Y. Huang, Y. P. Li, L. Yang, C. B. Wang, J. Liu, Y. H. Song, M. X. Yang and H. M. Li, *J. Colloid Interface Sci.*, 2021, **600**, 344–357.
24 C. Sun, L. Karuppasamy, L. Gurusamy, H.-J. Yang, C.-H. Liu, J. Dong and J. J. Wu, *Sep. Purif. Technol.*, 2021, **271**, 118873.
25 H. Xue, S. Xiong, K. Mi and Y. Wang, *Green Energy Environ.*, 2023, **8**, 194–199.
26 X.-R. Chen, W.-R. Cui, R.-P. Liang, C.-R. Zhang, R.-H. Xu, W. Jiang and J.-D. Qiu, *ACS Appl. Bio Mater.*, 2021, **4**, 6502–6511.
27 Z. Hu, Y. Wang, L. Wang, Q. Wang, Q. Zhang, F. Cui and G. Jiang, *Chem. Eng. J.*, 2024, **479**, 147534.
28 Y. Zhang, Z. Chen, Z. Shi, T. Lu, D. Chen, Q. Wang and Z. Zhan, *Sep. Purif. Technol.*, 2021, **275**, 119216.
29 S. Shang, H. Yang, D. Shi, B. Dong, H. Zhang, Q. Cheng and Z. Pan, *New J. Chem.*, 2021, **45**, 17025–17036.
30 J. Bi, Z. Zhang, J. Tian and G. Huang, *J. Colloid Interface Sci.*, 2024, **661**, 761–771.
31 Z. Li, S. Han, C. Li, P. Shao, H. Xia, H. Li, X. Chen, X. Feng and X. Liu, *J. Mater. Chem. A*, 2020, **8**, 8706–8715.
32 H. Vardhan, A. M. Al-Enizi, A. Nafady, Y. Pan, Z. Yang, H. R. Gutiérrez, X. Han and S. Ma, *Small*, 2021, **17**, 2003970.
33 Z. Liu and J. Wang, *J. Alloys Compd.*, 2020, **832**, 153771.
34 J. Wang, Z. Liu and Z. Liu, *Solid State Sci.*, 2019, **95**, 105935.
35 M. Wang, G. Tan, D. Zhang, B. Li, L. Lv, Y. Wang, H. Ren, X. Zhang, A. Xia and Y. Liu, *Appl. Catal., B*, 2019, **254**, 98–112.
36 Z. Liu and J. Xu, *Appl. Surf. Sci.*, 2020, **511**, 145460.
37 Y. Cong, Y. Ji, Y. Ge, H. Jin, Y. Zhang and Q. Wang, *Chem. Eng. J.*, 2017, **307**, 572–582.
38 L. Li, T. Chen, Z. Liu and P. Feng, *Mater. Lett.*, 2018, **212**, 267–270.
39 J. Xu, Y. Teng and F. Teng, *Sci. Rep.*, 2016, **6**, 32457.
40 H. Vardhan, Y. Pan, Z. Yang, G. Verma, A. Nafady, A. M. Al-Enizi, T. M. Alotaibi, O. A. Almaghrabi and S. Ma, *APL Mater.*, 2019, **7**, 101111.
41 H. Wang, D. Yong, S. Chen, S. Jiang, X. Zhang, W. Shao, Q. Zhang, W. Yan, B. Pan and Y. Xie, *J. Am. Chem. Soc.*, 2018, **140**, 1760–1766.
42 F. Guo, W. Shi, H. Wang, H. Huang, Y. Liu and Z. Kang, *Inorg. Chem. Front.*, 2017, **4**, 1714–1720.
43 J. Tian, P. Hao, N. Wei, H. Cui and H. Liu, *ACS Catal.*, 2015, **5**, 4530–4536.
44 X. M. Tu, S. L. Luo, G. X. Chen and J. H. Li, *Chem. – Eur. J.*, 2012, **18**, 14359–14366.
45 C. Martínez, M. Canle L, M. I. Fernández, J. A. Santaballa and J. Faria, *Appl. Catal., B*, 2011, **107**, 110–118.
46 E. Mugunthan, M. B. Saidutta and P. E. Jagadeeshbabu, *J. Photochem. Photobiol., A*, 2019, **383**, 111993.
47 X. Cheng, P. Wang and H. Liu, *J. Environ. Chem. Eng.*, 2015, **3**, 1713–1719.
48 K. C. Hui, W. L. Ang, W. Z. N. Yahya and N. S. Sambudi, *Chemosphere*, 2022, **290**, 133377.
49 V. C. Sarasidis, K. V. Plakas, S. I. Patsios and A. J. Karabelas, *Chem. Eng. J.*, 2014, **239**, 299–311.